

See discussions, stats, and author profiles for this publication at: <https://www.researchgate.net/publication/51602997>

# Ambient Surfactant less Synthesis, Growth Mechanism, and Size-Dependent Electrocatalytic Behavior of High-Quality, Single Crystalline Palladium Nanowires

ARTICLE *in* ACS NANO · AUGUST 2011

Impact Factor: 12.88 · DOI: 10.1021/nn202434r · Source: PubMed

---

CITATIONS

36

---

READS

409

## 4 AUTHORS, INCLUDING:



Christopher Koenigsmann

Fordham University

36 PUBLICATIONS 891 CITATIONS

[SEE PROFILE](#)



Alexander Santulli

Manhattan College

15 PUBLICATIONS 488 CITATIONS

[SEE PROFILE](#)

# Ambient Surfactantless Synthesis, Growth Mechanism, and Size-Dependent Electrocatalytic Behavior of High-Quality, Single Crystalline Palladium Nanowires

Christopher Koenigsmann,<sup>†</sup> Alexander C. Santulli,<sup>†</sup> Eli Sutter,<sup>‡</sup> and Stanislaus S. Wong<sup>†,§,\*</sup>

<sup>†</sup>Department of Chemistry, State University of New York at Stony Brook, Stony Brook, New York 11794-3400, United States, <sup>‡</sup>Center for Functional Nanomaterials, Brookhaven National Laboratory, Building 735, Upton, New York 11973, United States, and <sup>§</sup>Condensed Matter Physics and Materials Sciences Department, Brookhaven National Laboratory, Building 480, Upton, New York 11973, United States

One-dimensional (1D) metallic nanostructures, in particular, have garnered significant attention in the literature recently, owing to their unique structure-dependent optical, electrical, and thermal properties.<sup>1</sup> More importantly, 1D noble metal nanostructures, particularly those composed of Pt and Pd, have been highlighted by our group as well as others as effective catalysts for both the oxygen reduction reaction (ORR) and methanol oxidation reaction (MOR).<sup>2–4</sup> Currently, the low efficiency of contemporary polymer electrolyte fuel cells (PEMFCs) arises primarily from the slow kinetics of oxygen reduction on state-of-the-art carbon supported Pt nanoparticles (NP/C), resulting in an observed cathodic overpotential.<sup>5–9</sup> Nanoparticulate Pt catalysts possess relatively high numbers of defect sites and low-coordination atoms at their surface as a result of their zero-dimensional (0D) structure, rendering them less active toward ORR.<sup>9–11</sup> This reality necessitates high precious metal loadings of 0.15 to 0.25 mg/cm<sup>2</sup> for practical efficiencies to be achieved.<sup>12</sup>

By contrast, 1D nanostructures are characterized by their highly anisotropic structure and are expected to display highly active low energy crystalline facets and relatively few defect sites.<sup>13,14</sup> These structural elements can therefore impart improved ORR kinetics by delaying surface passivation of the catalyst with O and OH groups to higher potentials as compared with Pt NPs. Accordingly, there have been several reports in the literature highlighting a distinctive structure-dependent enhancement in ORR activity

**ABSTRACT** In this report, we utilize the U-tube double diffusion device as a reliable, environmentally friendly method for the size-controlled synthesis of high-quality, single crystalline Pd nanowires. The nanowires grown in 200 and 15 nm polycarbonate template pores maintain diameters of  $270 \pm 45$  nm and  $45 \pm 9$  nm, respectively, and could be isolated either as individual nanowires or as ordered free-standing arrays. The growth mechanism of these nanowires has been extensively explored, and we have carried out characterization of the isolated nanowires, free-standing nanowire arrays, and cross sections of the filled template in order to determine that a unique two-step growth process predominates within the template pores. Moreover, as-prepared submicrometer and nanosized wires were studied by comparison with ultrathin 2 nm Pd nanowires in order to elucidate the size-dependent trend in oxygen reduction reaction (ORR) electrocatalysis. Subsequently, the desired platinum monolayer overcoating was reliably deposited onto the surface of the Pd nanowires by Cu underpotential deposition (UPD) followed by galvanic displacement of the Cu adatoms. The specific and platinum mass activity of the core–shell catalysts was found to increase from  $0.40$  mA/cm<sup>2</sup> and  $1.01$  A/mg to  $0.74$  mA/cm<sup>2</sup> and  $1.74$  A/mg as the diameter was decreased from the submicrometer size regime to the ultrathin nanometer range.

**KEYWORDS:** palladium · nanowire · growth mechanism · platinum monolayer · electrocatalysis · oxygen reduction reaction

when 1D nanostructures are employed.<sup>15,16</sup> For example, enhanced specific activity was observed in a hierarchical membranous structure composed of Pt nanowires (NWs).<sup>17</sup> However, the high degree of aggregation contributed to a low mass activity in this case. With respect to Pd, significant electrocatalytic enhancements have been observed by Abruna and co-workers in the case of Pd nanorods prepared by the electrodeposition of Pd onto carbon supports, as compared with analogously prepared Pd NPs.<sup>18</sup> Our group has obtained similar results for ultrathin Pd NW/C composites, which show a nearly 2-fold increase in specific activity

\* Address correspondence to sswwong@notes.cc.sunysb.edu, sswwong@bnl.gov.

Received for review June 30, 2011 and accepted August 18, 2011.

Published online August 29, 2011  
10.1021/nn202434r

© 2011 American Chemical Society

when compared with their commercial Pd NP/C counterparts.<sup>19</sup> This distinctive structure-dependent activity has also been generalized to alloyed 1D nanostructures and enhancements have been observed for both PtPd<sup>20</sup> and PtFe<sup>21</sup> composite structures. In related work, we have further extended the concept of an observed structure-dependent enhancement to include highly active Pt monolayer shell–Pd core (Pt–Pd) nanostructures. Specifically, we have prepared ultrathin Pt–Pd NWs with diameters of ~2 nm, which have displayed outstanding surface area specific, platinum mass, and platinum group metal (PGM) mass activities of 0.77 mA/cm<sup>2</sup>, 1.83 A/mg<sub>Pt</sub>, and 0.55 A/mg<sub>PGM</sub>, respectively, which represent significant enhancements of approximately 2-fold in each category as compared with their optimized Pt–Pd NP counterparts.<sup>19</sup>

Although the structure-dependent enhancement observed with 1D noble metal nanostructures has been well documented, there have been very few reports that systematically correlate trends in physical structure and composition with electrocatalytic performance in the case of 1D nanostructures. For example, the rational exploration of size dependence in electrocatalysis is of great importance, since the size of the nanostructures determines the overall surface area-to-volume ratio and inevitably, the PGM loading. Recently, our group has studied size dependence in the case of 1D Pt nanostructures, wherein the activity of submicrometer nanotubes<sup>22</sup> with diameters of 200 nm was compared with that of the corresponding ultrathin ~1 nm Pt NWs.<sup>23</sup> A comparison of electrochemically determined specific activities revealed a nearly 4-fold increase in the specific activity from 0.38 to 1.45 mA/cm<sup>2</sup> as the 1D nanostructure diameter was decreased from the submicrometer range (*i.e.*, 100 nm < diameter <1 μm) to ultrathin (*i.e.*, < 5 nm) sizes. Surprisingly, the observed trend in the case of 1D catalysts starkly contrasts with that noted for analogous Pt NPs/C; in the latter case, the activity was found to decrease significantly as particle size was decreased from the submicrometer to ultrathin sub-5 nm levels. The overall enhancement observed in the Pt NW catalysts was believed to arise from a characteristic contraction of the ultrathin platinum NW surface, which had been previously observed experimentally and predicted theoretically.<sup>24–26</sup> Hence, the enhancement noted in ultrathin Pt NWs reveals that decreasing their size (i) minimizes the amount of wasted precious metal in the interior of the structure and (ii) results in an increase in observed activity.

Nevertheless, a continuing challenge in the exploration of size-dependent trends with 1D nanostructures, particularly those composed of Pd, has been the development of environmentally friendly methods for the generation of crystalline, high-quality nanostructures with high aspect ratios and predictable dimensions. For example, Xia and co-workers have

developed effective solvothermal-based methods for the preparation of anisotropic structures of Pd such as rods, plates, cubes, and twinned particles, wherein the rational control of the reaction kinetics in the presence of certain additives results in predictable morphologies.<sup>27</sup> The generation of high-quality nanowires and nanorods of Pd with diameters of 9.0 nm has been achieved hydrothermally by employing poly(vinylpyrrolidone) (PVP) as both a surfactant and an *in situ* reducing agent.<sup>28</sup> By contrast, several ambient solution-based techniques have also been proposed for the predictive preparation of ultrathin Pd NWs with diameters ranging from 2 to 6 nm. These protocols generally utilize surfactants as a means of directing the growth of Pd into 1D structures.<sup>29–32</sup> Recently, metallic NWs composed of Te<sup>33</sup> and Ag,<sup>20</sup> for example, have been used as sacrificial templates for the production of Pd NWs through galvanic displacement reactions. Similarly, templating of bimetallic PtRh and PtPd NWs can also be accomplished by utilizing either Rh or Pd nanocubes as seeds for the subsequent generation of Pt-forming NW networks.<sup>34,35</sup>

Although all of these methods can generate high-quality 1D Pd nanostructures, a key limitation of these synthetic protocols is that they do not readily afford rational control over the diameter and aspect ratio of the resulting nanostructure. In addition, organic surfactant molecules that serve as capping agents in these synthetic routes are typically strongly adsorbed onto the surfaces of the resulting nanostructures. This experimental reality can be particularly challenging when these as-prepared materials are employed as ORR electrocatalysts, because exposure of the bare surface is critical for high activity.<sup>19,36</sup> In light of these real and practical limitations, hard template-based techniques have become ubiquitous in the development of 1D nanostructures with appropriate size and shape control. Specifically, the size and morphology of the resulting nanostructures can be controlled by the physical geometry and dimensions of the originating template pore channels themselves.<sup>1,13,37–41</sup>

In the case of nanostructured metals, a common method for obtaining 1D structures is through electrodeposition of precursors within the spatial confines of either polycarbonate (PC) or anodic alumina (AAO) membranes. For example, arrays of Pd NWs with highly uniform diameters of 80 nm have been prepared by electrodeposition within the confines of an AAO template, possessing pore sizes of ~80 nm.<sup>42</sup> However, the electrodeposition process necessarily requires additional electrochemical equipment, the use of caustic reaction media, and in many cases, physical vapor deposition techniques to deposit a conductive metallic backing onto the template prior to deposition.<sup>38</sup> With growing concern over the potentially harmful environmental impacts of synthesizing nanostructures, a key consideration in the rational development of

nanostructured electrocatalysts is that synthetic protocols should be reasonably efficient, ambient, and inexpensive, as well as minimize the use of harmful precursors and processes.

In pursuing these generalized strategies, we have employed the U-tube double diffusion device as an ambient, surfactantless method for the reliable preparation of high-quality, diameter-controlled Pd NWs. Our U-tube device consists of two half-cells mutually separated by a commercial membranous template, which serves as the scaffold for the subsequent growth of 1D NWs. Examples have included metal tungstates, binary oxides, phosphates, sulfides, fluorides, and elemental metals.<sup>22,43–49</sup> Recently, the U-tube device has been highlighted for its versatility as both an effective and green method for the production of high-quality 1D metallic nanostructures under ambient conditions.<sup>50</sup> In the current report, we explore size-dependent electrocatalytic relationships in both elemental Pd NWs and Pt–Pd NWs possessing diameters that range from submicrometer to ultrathin <5 nm dimensions with the goal of further generalizing the size-dependent performance trend already observed in 1D Pt nanostructures.

Specifically, for the first time, we have employed the U-tube double diffusion device to prepare high-quality, *single crystalline*, submicrometer (270 nm) and nanosized (45 nm) Pd NWs. On the basis of careful analysis of partially formed NWs, we have gained important insight into the growth mechanism of the Pd NWs within the confines of PC templates. Subsequently, we have rationally explored the size-dependent electrochemical performance of both submicrometer and nanosized Pd NWs by comparison with ultrathin Pd NW/C composites obtained utilizing a surfactant-based technique that has been previously reported.<sup>19</sup> Ultimately, the desired Pt–Pd NW catalysts have been prepared by Pt monolayer deposition and the size-dependent ORR activity has been studied in these well-defined, diameter-controlled core–shell electrocatalysts. In both cases, we have observed consistently reproducible enhancements of 2-fold in terms of electrocatalytic activity as the diameter decreased from the submicrometer to ultrathin levels.

## RESULTS AND DISCUSSION

**Synthesis and Characterization of Pd NWs.** The synthesis of submicrometer and nanosized Pd NWs with highly monodisperse dimensions has been readily achieved by utilizing an ambient, surfactantless template-based method. The crystallinity and purity of the as-prepared NWs were characterized by powder X-ray diffraction data, shown in Figures 1A and 2A for the nanosized and submicrometer wires, respectively. Crystallographic analysis confirms that all of the peaks for the NWs prepared in templates composed of 200 nm (submicrometer) and 15 nm (nanosized) pores could be readily assigned to the (111), (200), (220), and (311)

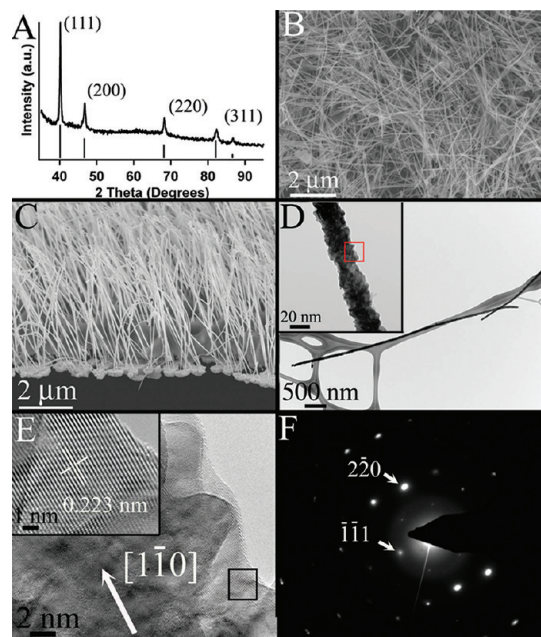


**Figure 1.** A representative powder X-ray diffraction pattern (A) of isolated 45 nm diameter Pd NWs. Representative SEM images of the isolated NWs (B) and of the free-standing NW array (C) after the PC template is removed. A low-resolution TEM image (D) of a single isolated NW with a section of the NW is shown as an inset. The red box denotes the area where a high-resolution image (E) was obtained. A selected area denoted by the black box highlighting the well-defined 111 lattice planes is shown as an inset to panel E. The selected area electron diffraction pattern (F) corresponding to the high resolution image is also highlighted.

reflections of face-centered cubic Pd (*Fm3m*, JCPDS No. 46-1043). The measured *d*-spacing for the (111) reflection of Pd of 2.243 Å isolated from the various template pores analyzed in these experiments is in excellent agreement with the standard value of 2.245 Å. In addition, there were no detectable crystalline impurities in the XRD pattern for either the submicrometer or the nanosized Pd NW samples.

The morphology of as-prepared NW samples was initially characterized by SEM. Overview scanning electron microscopy (SEM) images (Figures 1B and 2B) reveal that the NWs maintain diameters of  $45 \pm 9$  and  $270 \pm 45$  nm with high aspect ratios of  $73 \pm 22$  and  $13 \pm 4$ , for samples derived from the 15 and 200 nm template pores, respectively. The apparent size discrepancy between the commercially reported pore diameter and the experimentally measured diameter is expected and has been previously reported by our group as well as other groups.<sup>22,51</sup> This divergence has been widely attributed to an expansion and inhomogeneity of the diameter of pore within the interior of the membrane in combination with swelling of the pores during the growth of the NWs. In addition to obtaining individual isolated NWs, free-standing NW arrays, shown in Figures 1C and 2C, have also been readily obtained by affixing the filled templates onto a Si substrate and exposing the array to an oxygen plasma

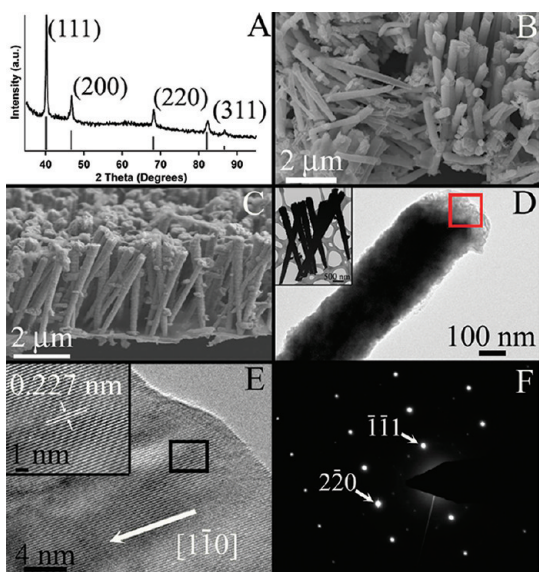


**Figure 2.** A representative powder X-ray diffraction pattern (A) of isolated 270 nm diameter Pd NWs. Representative SEM images of the isolated NWs (B) and of the free-standing NW array (C) after the PC template is removed. A low-resolution TEM image (D) of a single isolated NW with a representative collection of 270 nm diameter NWs is shown as an inset. The red box highlights the area where a high-resolution image (E) was obtained. A selected area denoted by the black box showing the well-defined 111 lattice planes is presented as an inset to panel E. A selected area electron diffraction pattern (F), corresponding to the high-resolution electron microscopy image, is also displayed.

etch in order to suitably remove the PC template. The highly uniform nature of the resulting arrays and the ability to affix them onto a wide variety of substrates have rendered these systems as excellent candidates for applications in hydrogen sensing<sup>52,53</sup> and alcohol electrooxidation.<sup>54</sup> The methods for obtaining both isolated NWs and free-standing NW arrays are shown schematically in Supporting Information, Figure S3.

Representative transmission electron microscopy (TEM) images shown in Figures 1D and 2D not only confirm the quality and high aspect ratio of the NWs but also reveal that the NWs maintain uneven, roughened surfaces, likely originating from the textured, imperfect structure of the pore walls of the PC template itself.<sup>49</sup> The high-resolution TEM images (HR-TEM) (Figures 1E and 2E) show that the NWs are single-crystalline, with the exception of a short polycrystalline segment at the end of the NW. The presence of this short polycrystalline segment can likely be attributed to the unique formation process of these NWs, which is discussed in greater detail in the following section. The high-resolution TEM images in Figures 1E and 2E indicate the presence of well-resolved lattice planes that are straight and equidistant with a spacing of  $2.25 \pm 0.03$  Å, in perfect agreement with the bulk Pd (111) lattice spacing. To assess the crystal structure over the entire length of the NW, we have employed electron diffraction in TEM. The diffraction patterns (DPs) taken along the length of the

NWs demonstrate that these NWs are single crystalline over the greater part of their length. Figures 1F and 2F show diffraction patterns obtained with the electron beam incident along the [112] axis of Pd. Diffraction data in combination with HRTEM images suggest that the long axis of the NWs formed in both the 200 and 15 nm pores is oriented along the [110] crystallographic direction. This unique growth direction of the Pd NWs has been observed previously when metallic NWs have been electrodeposited within highly anisotropic nanostructured pores. However, it is unclear in the existing literature as to which primary experimental influence ultimately determines the observed growth direction.<sup>55</sup> Given the lack of dependence on the pore size, we believe that the growth direction of these NWs arises from the relatively slow reduction kinetics observed in this synthetic scheme. This hypothesis is discussed in more detail in the following section.

Although there are many advantages of the U-tube methodology, the use of nanostructured templates may inherently prevent high product yields or even the acquisition of ultralow diameters, as the smallest commercially available PC template consists of  $\sim 15$  nm diameter pores. In light of these limitations, in parallel, we have prepared ultrathin Pd NWs utilizing a scalable wet-chemical technique wherein the reduction of a Pd precursor and growth is directed by a surfactant.<sup>19,29</sup> The as-prepared NWs in this case can be reliably supported onto high surface area carbon, which prevents aggregation of the NWs during treatment and imparts significantly improved durability. Low resolution TEM images of the ozone-treated ultrathin NWs shown in Supporting Information, Figure S1A reveal that the NWs maintain ultrathin diameters of  $2.2 \pm 0.8$  nm with lengths of up to 100 nm. Not surprisingly, overview field emission SEM (FESEM) images (Figure S1B) not only confirm the presence of ultrathin Pd NWs adsorbed onto the carbon but also highlight that the catalyst is uniformly distributed over the carbon surface. On the basis of the HRTEM images obtained before ozone treatment (Figure S1D), the NWs are composed of multiple single crystalline segments with lengths of  $6 \pm 1$  nm that extend along the entire length of the NWs. These single crystalline segments likely represent the electrochemically active structural unit of the NW since they maintain highly uniform, relatively defect-free surfaces. Crystallographic analysis of the NWs (Figure S1C) confirms that they are associated with the face-centered cubic phase of Pd. Moreover, there were no detectable crystalline impurity peaks.

**Insights into the Growth of Metallic Nanowires under Double Diffusion Conditions.** In addition to preparing optimized nanostructures for use as size-dependent core–shell electrocatalysts, we have also gained insight into the formation process of metallic NWs within the spatial boundaries and constraints associated with PC templates, under double diffusion conditions (Supporting

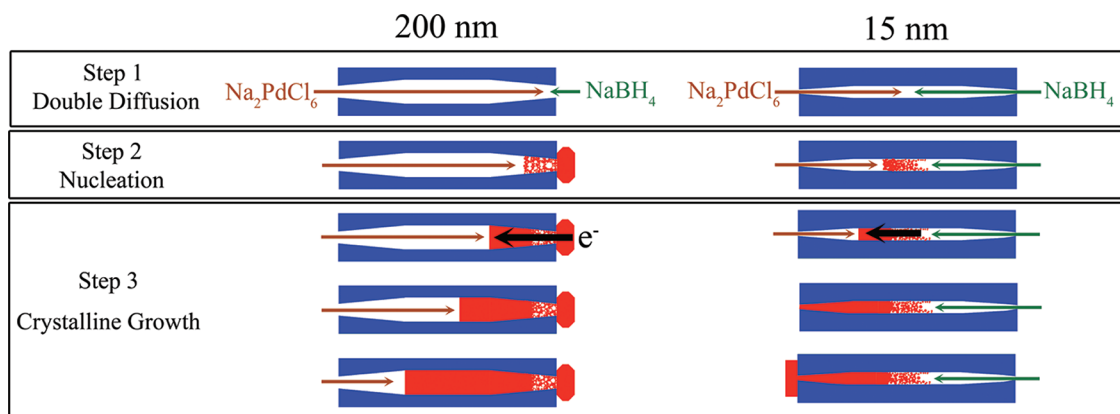


**Figure 3.** A schematic representation of the proposed formation process in a representative 200 nm (left) and 15 nm (right) diameter template pore. The left side of the graphic represents the precursor half-cell and the right side of the graphic denotes the reducing agent half-cell. In the double diffusion step, we highlight the difference in the point of nucleation that is observed in the case of the 200 and 15 nm template pores. In both cases, the growth is initiated by rapid nucleation of metallic Pd as the diffusion fronts of the precursor and reducing agent intersect within the template pores. Once the formation of the polycrystalline segments blocks the diffusion of the reducing agent into the pore, the growth of the primary single crystalline segments proceeds by an electrodeposition process where electrons are transported through the growing wire (black arrow). Observed metallic backing layers present on the external surfaces of the 200 and 15 nm templates are found on the reducing agent and precursor half-cell sides, respectively, and are shown in red.

Information, Figure S2). Previously, our group has achieved the reliable synthesis of metallic Au, Ag, and Pt NWs within the structural confines of 200 nm PC templates by utilizing relatively high concentrations of 0.1 and 0.5 M for the metal precursor and the sodium borohydride, respectively.<sup>22</sup> The Pt NWs prepared with the analogous H<sub>2</sub>PtCl<sub>6</sub> precursor in this previous report were found to be polycrystalline and the growth was determined to have followed a heterogeneous nucleation mechanism. Similarly, another group has prepared Ag NWs by utilizing a double diffusion device wherein a so-called “self propulsion mechanism” was proposed.<sup>56</sup> By contrast, the synthesis of Pd NWs in this report was accomplished with significantly lower concentrations of 37 mM Na<sub>2</sub>PdCl<sub>6</sub> and 5 mM NaBH<sub>4</sub> as a result of the inherently low solubility of the Pd precursor in ethanol. Interestingly, we find that the synthesis of Pd NWs is distinctive from that of other template-based syntheses conducted under similar double-diffusion conditions. In this section, we rationally explore the growth mechanism in the 200 and 15 nm template pores utilizing complementary techniques that provide insight into the structure and location of the NW within the template pore as the reaction progresses.

**Growth of Pd NWs within 200 nm Pores.** On the basis of the analysis of our data, we believe that the growth of the NWs within the PC templates follows a two-step process, which is shown schematically in Figure 3. In the first step, the precursor and reducing agent diffuse into the pore space and inevitably, the diffusion fronts intersect, resulting in the reduction of the Pd precursor and nucleation of the Pd metal. In the case of the 200 nm template pores, the nucleation of the Pd metal is initiated near the interface of the template pore and reducing agent half-cell. This initial rapid reduction

followed by a nucleation process yields both a short polycrystalline NW segment within the template pore and a thin layer of metallic material on the outer surfaces of template within the reducing agent half-cell. In fact, the formation of the metallic layer on the surface of the template facing toward and thereby exposed to the reducing agent half-cell can be observed visually within the first minute of the reaction. As complementary evidence, TEM analysis of a representative cross-section of the template shown in Figure 4A confirms the presence of a thin metallic layer localized on the external surface of template that is exposed to the reducing agent half-cell with NWs that are directly affixed onto the metallic layer. Higher magnification images reveal that the first 500 nm of the NW affixed to the metallic layer is composed of highly interconnected crystalline grains.

To explore the crystallinity of the NW near the interface of the template pore, HRTEM images and SAED patterns (Figure 4B) were obtained on a representative isolated Pd NW at positions near the pore interface where it is thought that nucleation first occurs. The corresponding HRTEM images reveal that the polycrystalline segment is composed of multiple crystalline domains that give rise to the distinctive diffraction rings in the SAED pattern. Based upon the low-resolution and high-resolution TEM images, the polycrystalline component represents the first 200–500 nm of the NW, which is directly affixed onto the metallic material, coating the exterior of the template. The observation of the initial polycrystalline segment is not surprising since we have previously demonstrated that the direct reduction of metallic precursors, including H<sub>2</sub>PtCl<sub>6</sub> for example, results in polycrystalline nanostructures.<sup>22</sup> The polycrystallinity arises from the rapid reaction

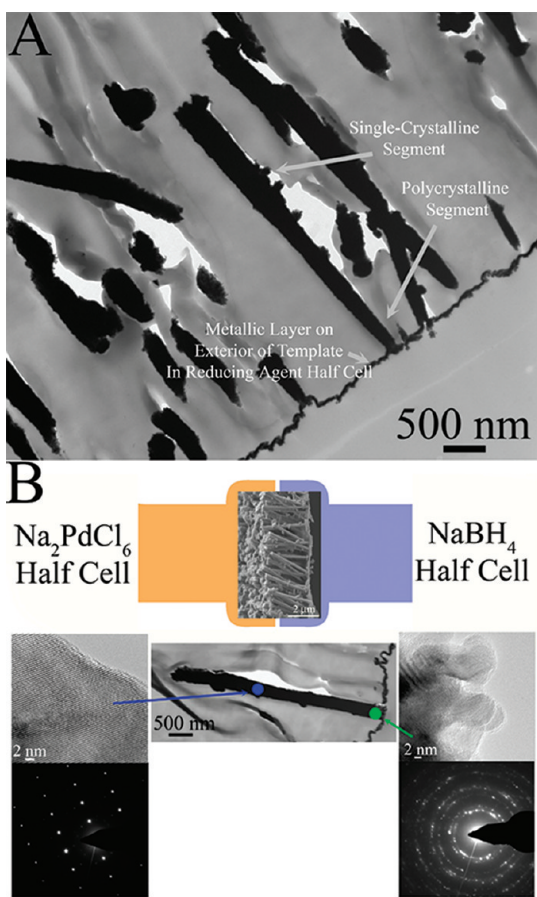


**Figure 4.** Representative cross-section of as-prepared templates containing  $\sim 270$  nm (A) NWs after 16 min of reaction time. The presence of wire-like fragments results from the nonuniformity and irregular distribution of the template pores, which results in portions of wires being excised during the microtoming process. Cross-sectional SEM images of free-standing NWs prepared in the 200 nm (B) diameter pores of PC templates shown within a schematic of the U-tube double-diffusion apparatus. The metallic layers present on the surfaces of the 200 nm templates are found on the reducing agent half-cell side. Immediately below are individual NWs within the template pore with corresponding HRTEM and SAED patterns obtained from a representative, isolated Pd NW in selected locations marked by blue and green spots, where either nucleation or crystalline growth predominate.

kinetics when  $\text{NaBH}_4$  directly interacts with and reduces the metal precursor, a process which favors the formation of many discrete nuclei as opposed to simple crystalline growth. Hence, we propose that the polycrystalline segment arises in the first growth step from the rapid nucleation of Pd metal when there is direct chemical interaction between the diffusing Pd precursor and the  $\text{NaBH}_4$  solution.

Interestingly, careful analysis of the cross-sectional images reveals that the polycrystalline segment transforms into a uniform homogeneous segment toward the interior of the template pore. HR-TEM images and SAED patterns obtained on a representative NW toward the interior of the pore confirm that this segment of the wire is single crystalline with highly resolved

lattice planes that run uniformly across the entire structure. This gives rise to the well-defined diffraction spots present on the corresponding SAED. Hence, the short polycrystalline segment segues into a second single crystalline segment that comprises the remaining 3–4  $\mu\text{m}$  of the NW. However, the extended single-crystalline segment that is observed extending toward the precursor half-cell is not necessarily consistent with the idea of the direct reduction of Pd by  $\text{NaBH}_4$ . By contrast, these findings imply that a different growth process likely predominates in creating this single crystalline segment.

Hence, we believe that the single-crystalline growth observed in the template pore arises from a second, *in situ* electroless deposition process wherein the rate of reduction is significantly slowed. We believe this allows for crystalline growth to predominate as opposed to a series of rapid nucleation steps. Invariably, the formation of the aforementioned polycrystalline material and metallic layer prevent the direct diffusion of precursor and borohydride ions into the template pores, thereby preventing the direct reduction of Pd. Subsequently, we believe the thin metallic layer and polycrystalline segment serve as a conductive layer through which electrons are transported from the reducing agent half-cell toward the interior portion of the pore, thereby reducing the Pd precursor. This in turn results in the lengthening of a distinctive single crystalline segment toward the precursor half-cell.

As a matter of note, we believe that electrochemical neutrality is maintained during the electroless deposition process by the corresponding diffusion of positive  $\text{Na}^+$  ions from the reducing agent half-cell into the precursor half-cell. Previously, it was proposed by Sharabani *et al.* in their study of the electroless deposition of Ag NWs under double diffusion conditions that the diffusion of  $\text{Na}^+$  ions occurs through the physical spaces present between the growing NW and the surrounding pore walls.<sup>56</sup> Moreover, it has been demonstrated that the pore spaces of the PC templates are nonuniform and that pore branches exist throughout the template. These dispersed spaces may represent possible channels and physical pathways for the diffusion of counterions.<sup>51</sup> Although all of these scenarios exist as plausible routes for  $\text{Na}^+$  ion diffusion, it is critical to highlight that the determination of the precise mode of counterion diffusion is beyond the scope of this report and will be addressed in the future.

Recently, single-crystalline Pd NWs have been grown within nanostructured templates using a potentiostatic electrodeposition process involving careful control over the pore size and the reduction overpotential.<sup>55</sup> It was found in that experiment that reducing the pore size from 65 to 35 nm and utilizing a low reduction overpotential (0.3 V vs Ag/AgCl) favored the growth of single crystalline NWs as opposed to polycrystalline NWs. The smaller pore sizes in combination with a

slower reaction rate were thought to limit the diffusion in the system, thereby lowering the reaction rate and promoting single crystalline growth. On the basis of these prior results, as well as the HR-TEM and SAED results, we believe that the growth of the single-crystalline NW segment herein arises from an ambient, electroless deposition process that is primarily diffusion-limited. This assertion is consistent with the proposed mechanism due to inherent coupling between the reaction rate and the diffusion rate of both the precursor into the pores and the  $\text{Na}^+$  ions into the precursor half-cell.

As experimental evidence of the proposed second electrodeposition step, we isolated free-standing NW arrays after various reaction times (4–16 min) to confirm that the NW elongates toward the precursor half-cell over the course of the reaction. In this case, the free-standing arrays were prepared by supporting the templates onto Si substrates, and the residual PC is removed by a reactive oxygen plasma etching process leaving behind the NWs directly affixed to the thin metallic layer (Supporting Information, Figure S3). On the basis of the proposed growth mechanism, the length of the NWs is expected to increase at longer reaction times, owing to prolonged electrodeposition periods. SEM images of the arrays grown in the 200 nm templates after 4, 8, and 12 min of reaction time are shown in Figure S4A–S4C, and not surprisingly, these as-prepared 1D nanostructures increase in length from approximately 2 to over 3  $\mu\text{m}$  as the reaction time is increased from 4 to 16 min. To gain a more quantitative insight, these as-prepared 1D nanostructures were isolated as individual NWs (Figure S3) from reactions conducted in 2 min increments and the length was found to increase from  $0.92 \pm 0.35$  to  $4.0 \pm 1.8 \mu\text{m}$  (Figure S5A) as the reaction time was correspondingly increased from 2 to 12 min, thereby representing almost the entire thickness of the template ( $\sim 6 \mu\text{m}$ ). Hence, it is clear that the growth of the NWs continues even after the initial polycrystalline segment effectively prevents direct interaction between reducing agent and precursor molecules. These observations are collectively suggestive of a second, continuous electrodeposition step.

**Growth of Pd NWs within 15 nm Pores.** The growth of the NWs in the 15 nm template pores follows a similar two-step process that is observed within the 200 nm template. However, a key distinction in the formation of the NWs in the 15 nm pores is that the initial nucleation of the Pd likely occurs within the interior of the pore (near the center of the pore channel), as opposed to at the interface of the pore with the reducing agent half-cell. TEM images of cross sections of the template (Figure 5A) in addition to HRTEM analysis (Figure 5B) of a representative isolated NW confirm the presence of a polycrystalline segment located toward the center of the template pore. The shift in the location

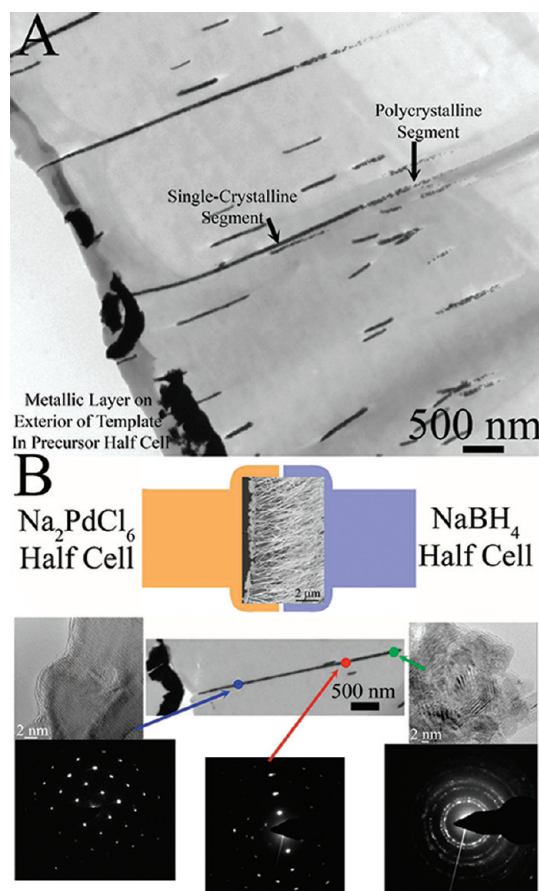


**Figure 5.** Representative cross-section of as-prepared templates containing  $\sim 15$  nm (A) NWs after 16 min of reaction time. The presence of wire-like fragments arises from the nonuniformity and irregular distribution of the template pores, which results in portions of wires being excised during the microtoming process. Cross-sectional SEM images of free-standing NWs prepared in the 15 nm (B) diameter pores of PC templates shown within a schematic of the U-tube double-diffusion apparatus. The metallic layers present on the surfaces of the 15 nm pore-sized templates are found on the precursor half-cell side. Immediately below are individual NWs within the template pore with corresponding HRTEM and SAED patterns obtained from a representative, isolated Pd NW in selected locations marked by blue, red, and green spots, where either the nucleation or the crystalline growth predominate.

of the nucleation process likely arises from the smaller pore size, which is expected to significantly limit the diffusion of the precursor into the pore space.<sup>57,58</sup> On the basis of the cylindrical pore geometry, the point of contact between advancing diffusion fronts of the precursor and reducing agent is thereby expected to shift toward the interior of the pore and give rise to a primary nucleation process occurring closer toward the precursor half-cell. To explore this issue more rationally, we performed a series of reactions (cf. Supporting Information and Figures S5B – S5C) wherein the precursor and reducing agent concentrations were altered systematically to explore the influence of diffusion rate upon the corresponding length of the wire. Not surprisingly, the length of the resulting wires can be

rationally increased when the precursor concentration is increased. This confirms that the position where primary nucleation likely occurs is highly dependent upon the nature of the diffusion of the precursor in this case.

Subsequently, HR-TEM analysis of the NWs at points closer toward the precursor half-cell confirms that the polycrystalline segment transitions into an extended single-crystalline segment. As in the case of the 200 nm NWs, we believe that the single-crystalline segment arises from a second electrodeposition step, occurring once the pore space is spatially blocked by the formation of the initial polycrystalline segment. However, an interesting distinction in this case is that the crystalline growth of the NW proceeds beyond the pore, forming a metallic layer that coats the surface of the template in the precursor half-cell. This scenario is readily apparent in Figure 5A, which highlights the presence of metallic material on the surface of the precursor side of the template that is directly affixed onto the NWs within the template. The morphology of this film is apparent in Supporting Information, Figure S4D–F and it is evident that the film is composed of interconnected Pd material that extends beyond the template pores. In fact, visual observation of the template during the course of the reaction reveals that the template darkens from a transparent coloration to a black coloration over the first 2–4 min of the reaction and then a metallic layer becomes apparent on the surface of the template in the precursor half cell after 4–6 min.

As further support for the proposed growth mechanism, we have isolated free-standing NW arrays after various reaction times (4–16 min) to confirm that the NW growth direction proceeds from the point of nucleation toward the precursor half-cell. In this case, the templates were affixed onto a Si substrate with the metal-coated precursor side facing downward, and the residual PC was removed by reactive ion etching in an oxygen plasma, utilizing the same etching conditions as those for the 200 nm pores. SEM images of arrays obtained after 4, 8, and 12 min of reaction time are highlighted in Figure S4D–F. Analysis of the NW arrays reveals that the length of the NWs does not change significantly from 4 min ( $2.9 \pm 0.6 \mu\text{m}$ ) to 16 min ( $2.8 \pm 0.6 \mu\text{m}$ ). In this case, the growth of the NWs from the point of nucleation to the pore opening appears to have been completed within the first 4 min of the reaction, which is consistent with the empirical observation of the formation of the metallic material within a 4–6 min interval on the surface of the template in the precursor half-cell. Interestingly, the filling of the pore proceeds at a much faster rate in the 15 nm pores as compared with the 200 nm pores, which is not surprising given that the reaction rate is the same in both the 15 and 200 nm pores, although less Pd is obviously required to fill in the smaller pores. Hence, all of these observations complement the analysis of the template

cross-section and confirm that the growth is likely initiated within the interior of the pore space and then proceeds toward the precursor half-cell, inevitably producing a metallic layer on the surface of the template exposed to the precursor half-cell.

**Size-Dependent ORR Activity of Pd NWs.** Prior to systematic electrochemical characterization of the various Pd NW samples, the surfaces of the NWs were activated in order to remove undesirable organic residues. In the case of the submicrometer-sized and nanosized wires prepared in the U-tube assembly, the residual organic material left from remnants of the PC membrane could be readily removed from the NWs on the electrode by briefly cycling to high potentials (~1.3 V). This experimental capability highlights the highly advantageous nature of U-tube synthetic methods since NWs with high aspect ratios can be prepared rapidly without the need for surfactant, which can significantly hinder electrochemical performance. By contrast, the ultrathin Pd NW/C sample required a more complex two-step cleaning process that involved the combination of pretreatment and electrochemical protocols in order to remove strongly adsorbed octadecylamine (ODA) surfactant.<sup>19</sup>

Once the surfaces of the NWs were suitably activated, the electrochemical performance of the NWs was initially explored by cyclic voltammetry. Specifically, cyclic voltammograms (CVs) obtained in a 0.1 M HClO<sub>4</sub> solution (Figure 6A) evinced the distinctive hydrogen adsorption/desorption ( $H_{\text{ads}}$ ) peaks in the region of 0–0.2 V and the onset of surface oxide formation at approximately 0.7 V, which are consistent with that of nanostructured Pd catalysts. Not surprisingly, the CV profile of the Pd NWs was in excellent agreement with that of commercial Pd NPs (Figure S6). The electrochemical surface area (ESA) of the various NW catalysts was determined in this case by integration of the CO stripping peak (Figure 6B). The CO stripping charge is used (*cf.* Supporting Information) to estimate surface area because in the case of Pd, the absorption of hydrogen into the lattice of Pd can contribute significantly to the measured  $H_{\text{ads}}$  charge, thereby making it unreliable for the accurate determination of surface area.

To explore the ORR activity of the submicrometer and nanosized Pd NWs, polarization curves shown in Figure 6C for the submicrometer and nanosized wires and Supporting Information, Figure S7 for the ultrathin NWs were obtained in oxygen-saturated 0.1 M HClO<sub>4</sub> solutions. These polarization curves revealed that the NW samples maintained an ORR onset in the region of 0.85–0.95 V, which is consistent with that found for other nanostructured Pd catalysts. More importantly, the kinetic currents were extracted at 0.8 V and normalized to the ESA in order to probe the specific activity (shown in the inset of Figure 6C) of the catalysts. In this case, we have elected to utilize the kinetic currents at 0.8 V, since the catalysts show insignificant activity

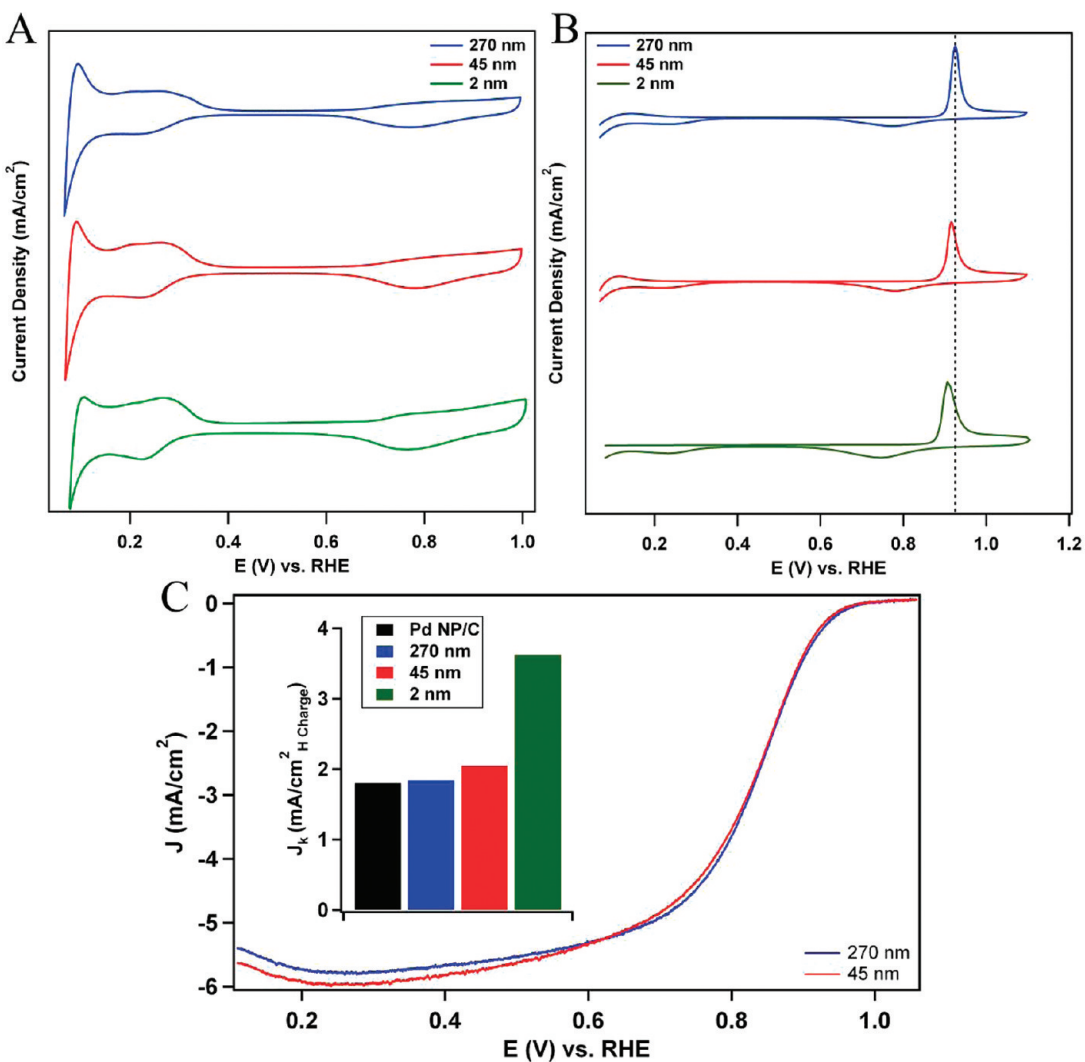


**Figure 6.** Cyclic voltammograms (A) and CO stripping voltammograms (B) of the submicrometer and nanosized Pd NWs by comparison with the ultrathin Pd NW/C composites obtained in deoxygenated 0.1 M  $\text{HClO}_4$  at 20 mV/s. Polarization curves (C) obtained from the submicrometer and nanosized Pd NWs immobilized on a Vulcan XC-72 modified GCE. Curves (anodic sweep direction) were obtained in an oxygen-saturated 0.1 M  $\text{HClO}_4$  solution at 1600 rpm and 20 °C with a scan rate of 10 mV/s. The electrochemical surface area activities (specific activities) of the submicrometer and nanosized Pd NWs at 0.8 V are shown as an inset by comparison with the ultrathin Pd NW/C catalysts and commercial Pd NP/C catalysts.

above 0.85 V. On the basis of this protocol, we have found that the measured specific activity doubles from 1.84 to 3.62  $\text{mA}/\text{cm}^2$  as the catalyst size is decreased from 270 to 2 nm. It is also important to highlight that all of our NW catalysts, particularly the 45 and 2 nm Pd NWs, consistently and reproducibly out-perform a commercial Pd NP/C catalyst, which showed a specific activity of 1.80  $\text{mA}/\text{cm}^2$ .

The observed electrochemical enhancement in the Pd NW samples when compared with the commercial Pd NP samples is not surprising since our group and others have previously shown in the case of both Pt and Pd, that 1D catalysts maintain significantly more active surfaces as compared with analogous NPs.<sup>2,18,19,23</sup> Although there is some debate in the literature,<sup>18</sup> analysis of ORR activity on Pd single crystals<sup>59</sup> and well-defined Pd nanocubes<sup>60</sup> has shown that the Pd (100) facet is significantly more active than the Pd (111)

facet. Consistent with this assertion, we have previously demonstrated by HRTEM that our ultrathin NWs primarily display Pd (100) facets as a result of the selective adsorption of octadecylamine onto this surface during NW growth.<sup>19</sup> Hence, the significantly enhanced activity of our ultrathin Pd NWs is understandable, since commercial Pd NPs display predominantly Pd (111) facets.<sup>60</sup>

Although the structure-dependent enhancement in ORR activity has been previously explored, the distinctive size-dependent enhancement specifically observed in this report is of critical interest, since activity tends to be enhanced with decreasing NW diameter. This trend starkly contrasts with analogous behavior observed in 0D NP catalysts, wherein decreases in size tend to result in lower activity as a result of an increased defect density as well as changes to the electronic structure of the catalysts.<sup>61</sup> Previously, we

have observed a similar size-dependent enhancement in analogous Pt NW catalysts wherein the specific activity increased from 0.38 to 1.45 mA/cm<sup>2</sup> in progressing from 200 nm Pt NTs to ultrathin ~1 nm Pt NWs.<sup>23</sup> Hence, the size-dependent performance enhancement appears to be quite generalized in the case of elemental metal 1D ORR catalysts.

We believe that this size-dependent enhancement in activity arises from a contraction of the Pd surface with decreasing size. There have been several previous theoretical<sup>25,62,63</sup> and experimental<sup>26,64</sup> reports that have shown that noble metal NWs such as Pt and Pd can undergo a contraction of the surface as the diameter is decreased into the nanoscale region, particularly when the diameter approaches that of approximately 2 nm. Contractions of the NW surface are expected to result in a down-shift in the *d*-band center of the material to lower energies. Such a situation is expected to weaken the binding of oxygen and to increase the rate of oxygen reduction.<sup>5,65–69</sup> Recently, X-ray photoelectron spectra (XPS) data collected on ultrathin 2 nm Pt NW catalysts have revealed that the Pt NWs maintained lower electron binding energies for the Pt 4f<sub>7/2</sub> signal as compared with commercial Pt NP catalysts, thereby providing further experimental evidence for a down-shift in the *d*-band energy of nanoscale 1D materials.<sup>70</sup>

As support for the proposed contraction in the case of Pd, we have obtained CO stripping voltammograms (Figure 6B) for the various Pd NW catalysts tested. In effect, the proposed down-shift of the *d*-band center due to surface contracting strain is expected to weaken the CO binding strength and to improve its surface diffusion rate, which may lead to an improvement in CO monolayer oxidation kinetics.<sup>71,72</sup> As expected, the CO stripping peak did shift negatively from 0.925 to 0.906 V as the size of the NWs was decreased from 270 to 2 nm, which suggests that there is improved CO oxidation kinetics as the size of the NWs decreases. Hence, we believe that the trend in the CO stripping peak potential coupled with the recent XPS analysis of ultrathin Pt NWs provides strong evidence for a surface reconstruction process and a corresponding down-shift in the *d*-band energy as the size of the NWs is decreased. Separately, the improved CO oxidation kinetics observed also highlights the fact that ultrathin Pd NW/C composites are potentially effective catalysts for alcohol electro-oxidation.

We should emphasize that variations in the crystalline facets likely do not play a significant role in the size-dependent electrocatalytic enhancement of the as-prepared NWs observed in this report. It has been previously shown that Pd NWs and NPs that preferentially display different surface facets (e.g., either primarily (110) or a combination of (111) and (100) facets, respectively) maintain significantly different Cu UPD and CO stripping profiles, an observation that could be readily ascribed to the CO stripping profiles obtained with the corresponding Pd single crystals.<sup>18</sup> By contrast, the structure of the

Cu UPD and CO stripping profiles of our as-prepared NWs of various diameters remain largely identical with the exception of the shift in peak potential, suggesting that these NWs possess similar surface facets. Hence, the shift in the CO stripping peak potential in combination with the recent XPS data point toward surface contraction as the main origin of the observed electrocatalytic enhancement in NW activity herein. Although it is beyond the scope of this work, further exploration of the surface structure will be useful in fully ascertaining the origin of the observed size-dependent electrocatalytic activity in these 1D nanoscale materials.

#### Size-Dependent ORR Activity of Core–Shell Pt–Pd NWs.

Although the size-dependent ORR activity of elemental catalysts has been previously studied in the case of Pt, there have been no reports, to the best of our knowledge, exploring the size-dependent activity in 1D nanostructured core–shell Pt monolayer-based catalysts. However, determination of the size and structure dependent properties of these highly active, hierarchical structures is a critical step toward optimizing their performance for applications in working fuel cells. In this case, we utilized the well-defined Pd NWs from the previous section as substrates for Pt monolayer deposition in order to develop size-controlled 1D Pt monolayer–Pd nanowire core–shell (Pt–Pd NW) catalysts for the purpose of studying the size-dependence electrocatalytic activity in these structures.

In the current report, the deposition of a Pt monolayer onto the surface of the various Pd NWs was achieved by first depositing a monolayer of Cu onto the surface by Cu UPD followed by galvanic displacement of the Cu adatoms with Pt<sup>2+</sup>. Cyclic voltammograms obtained after the Pt monolayer deposition process (Figure 7A) confirmed that a nearly complete monolayer of Pt was deposited onto the surface. Specifically, the CVs of the Pt–Pd NWs showed a shift in the oxide region toward higher potentials as compared with the CVs of the Pd NWs. Moreover, the H<sub>ads</sub> region of the Pt–Pd NWs resembled that of the bulk Pt (111). The observed changes in the CV highlight the presence of a nearly contiguous monolayer of Pt at the Pd surface since the features closely resemble that of bulk Pt (111).<sup>66,68,69</sup> More importantly, we also observed that the potential of the surface oxide reduction peak shifts from 0.788 to 0.803 V, as the diameter of the NWs is decreased from 270 to 2 nm. A shift in the surface oxide feature to higher potentials is consistent with a weakening of the interaction between the metal surface and the oxygen adsorbate. Based upon the density functional theory (DFT) results of Nørskov and co-workers,<sup>5,73</sup> the observed weakening of the interaction with the oxygen adsorbate is consistent with a down-shift in the Pd *d*-band toward lower energies, a scenario which is likely expected to improve oxygen reduction kinetics.

The ORR activities of the submicrometer and nanosized Pt–Pd NWs were measured electrochemically by

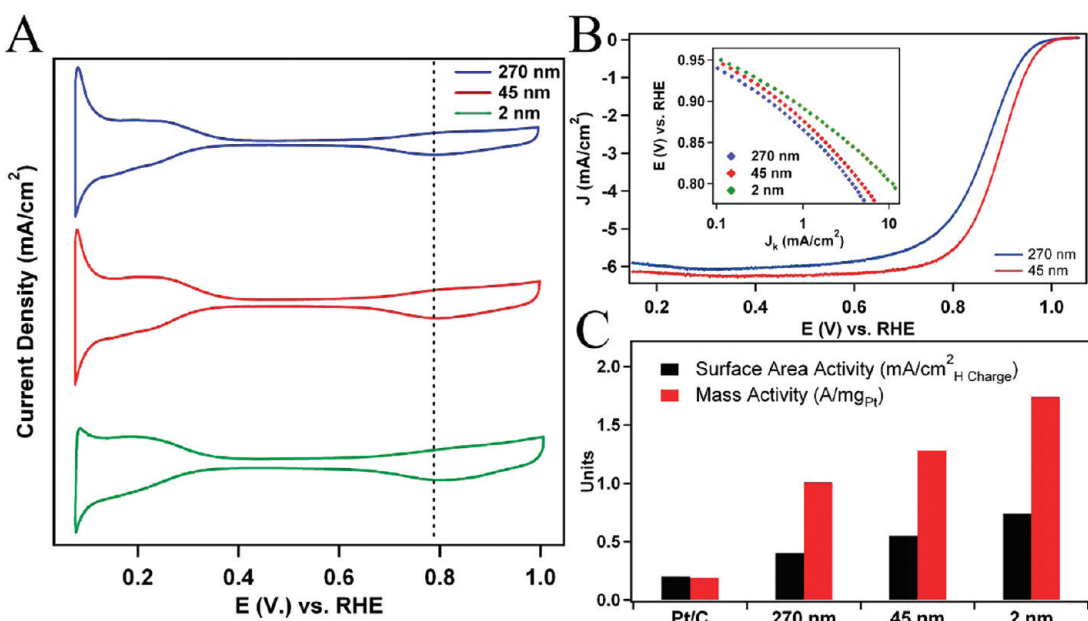


**Figure 7.** Cyclic voltammograms (A) obtained after Pt monolayer deposition of the submicrometer and nanosized Pt–Pd NWs by comparison with ultrathin Pt–Pd NW/C composites. The CVs were obtained in a deoxygenated 0.1 M  $\text{HClO}_4$  solution at 20 mV/s. Polarization curves (B) of the submicrometer and nanosized Pt–Pd NWs obtained on the NWs immobilized on a Vulcan XC-72 modified GCE. Curves (anodic sweep direction) were obtained in an oxygen saturated 0.1 M  $\text{HClO}_4$  solution at 1600 rpm and 20 °C with a scan rate of 10 mV/s. A potential vs specific activity plot ( $J_k$ ) is shown as an inset, corresponding to ultrathin Pt–Pd NW/C, noted as a comparison. The electrochemical surface area activity (ECSCA,  $\text{mA}/\text{cm}^2$ ) and the mass activity ( $\text{A}/\text{mg}_{\text{Pt}}$ ) at 0.9 V for the Pt–Pd NW samples are shown (C) by comparison with the ultrathin Pt–Pd NW/C composites and commercial Pt NPs/C.

obtaining polarization curves in an oxygen-saturated 0.1 M  $\text{HClO}_4$  solution shown in Figure 7B. As expected, the core–shell NWs maintain significantly enhanced activity as compared with the Pd NWs before monolayer deposition, which further confirms the near monolayer deposition of Pt. In this case, the specific activity of the Pt–Pd NW was determined by normalizing the measured kinetic currents obtained at 0.9 V to the measured ECSCA of the core–shell NWs, which can be directly deduced from integration of the  $H_{\text{ads}}$  peaks of the composite structure. Similarly, the Pt mass activity can be readily obtained by normalizing the measured kinetic current at 0.9 V to the mass of Pt deposited, which can itself be determined from the Cu UPD profiles.

In this report, we are concerned with elucidating the size-dependent catalytic properties in 1D nanostructures and thus, the specific activity and the Pt mass activity are highlighted, because these are directly related to the number and density of active sites present on the catalysts tested. In accordance, we have summarized the average specific activity and platinum mass specific activity of the submicrometer, nanosized, and ultrathin Pt–Pd NWs obtained from three separately prepared electrodes in Figure 7C, with commercial Pt NPs/C serving as a comparison. The measured area specific and mass specific activities were found to increase from 0.40  $\text{mA}/\text{cm}^2$  and 1.01  $\text{A}/\text{mg}$  to 0.74  $\text{mA}/\text{cm}^2$  and 1.74  $\text{A}/\text{mg}$ , respectively, as the measured NW diameter was decreased from 270 to

2 nm. A potential versus kinetic current plot presented as an inset to Figure 7B reveals that the size-dependent enhancement in activity is observed over the entire range of plausible operating potentials for a fuel cell cathode.

In a recent report by Adzic and co-workers, the ORR activity was studied as a function of particle size in 0D nanoparticulate core–shell catalysts, and it was found that the measured activity decreases as the particle size is decreased below 10 nm, a finding consistent with those of elemental metal nanoparticles.<sup>66</sup> By contrast, the activity data in the case of 1D core–shell nanostructures are again in direct contrast with the trend observed for 0D catalysts. Specifically, the size-dependent phenomenon observed for 1D catalysts is extremely advantageous since greatly enhanced activities can be achieved by decreasing the diameter of the catalyst. Hence, coupling the increased activity of ultrathin NW catalysts with their high surface area-to-volume ratio maximizes the precious metal loading and decreases the amount of inactive precious metal present in the core of the nanostructure. In fact, the ultrathin 2 nm Pt–Pd NW composites have been shown to maintain a high total PGM mass activity of 0.55  $\text{A}/\text{mg}$ .

In addition, we have demonstrated that the size-dependent electrocatalytic enhancement observed in elemental Pt and Pd can be generalized further to that of core–shell 1D nanostructures. Specifically, as with Pd NWs, we believe that the performance enhancement in the case of the Pt–Pd NWs arises from a

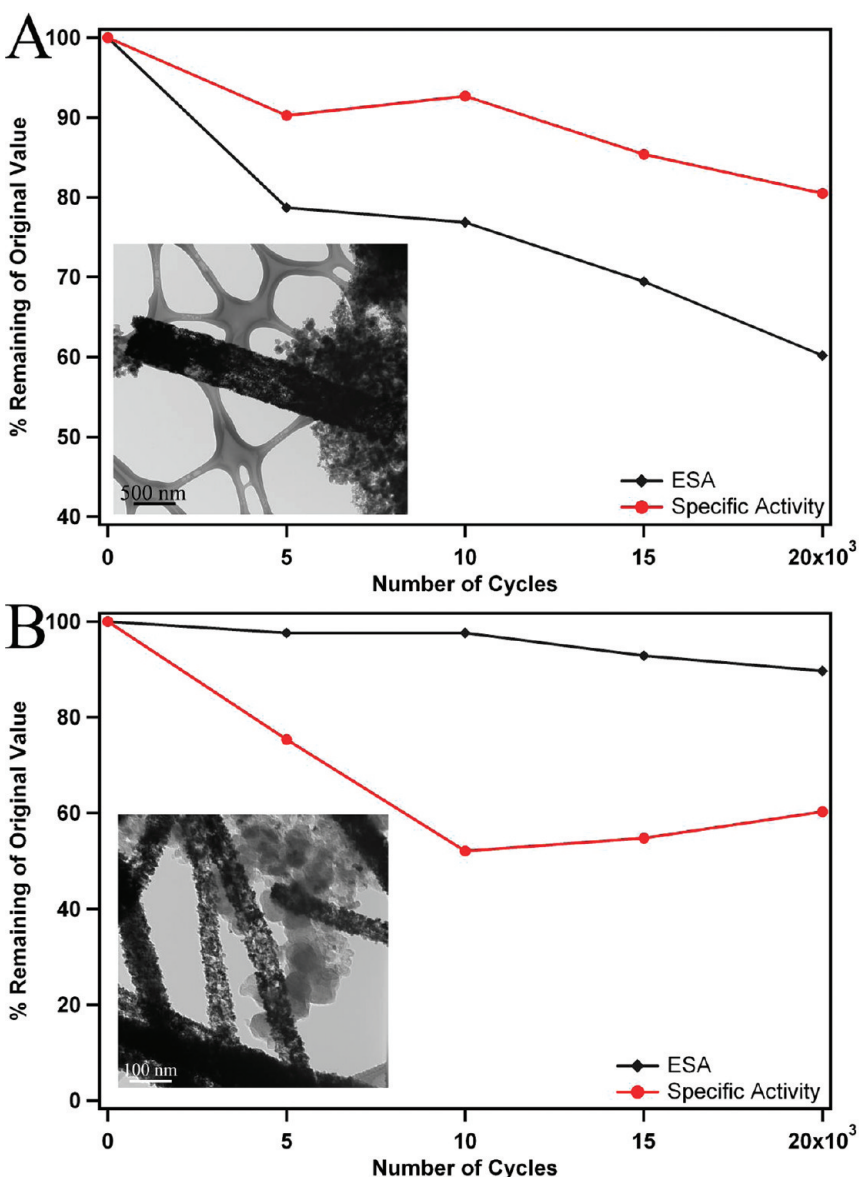


**Figure 8.** Durability results for the submicrometer (A) and nanosized (B) Pd NW samples, shown as the percentage of remaining ESA (black) and specific activity (red) over the course of 20 000 cycles. Also shown as insets are representative TEM images of the nanostructures collected after 20 000 cycles of processing.

diameter-dependent contraction of the Pd NW surface. Moreover, the enhancement in the ORR activity of the Pt monolayer supported on both Pd NP and single crystal surfaces is believed to arise from a strain-induced compression of the Pt monolayer in combination with a so-called electronic “ligand effect”.<sup>74</sup> On the basis of the results presented in the previous section, the use of 1D catalysts possessing a diameter-dependent surface contraction as substrates for Pt monolayer deposition is expected to increase the strain-induced effect upon the Pt monolayer and yield a corresponding increase in the ORR activity. This effect is also apparent in the CV results presented in Figure 7A, wherein the potential of the surface oxide reduction peak shifts to higher potentials as the size is decreased. That is, an increase in the strain-induced contraction of

the Pt monolayer is expected to result in a shift of the Pt *d*-band to lower energies and thereby weaken the interaction with surface adsorbates, such as oxygen.

**Durability Testing of Submicrometer and Nanosized Pt–Pd NWs.** The electrochemical durability of the submicrometer and nanosized Pt–Pd NWs was explored under half-cell conditions designed to simulate a catalyst lifetime. The primary motive for studying the stability of these model catalysts is to verify that they maintain their structural integrity and function during electrochemical testing. In this report, we utilize an electrochemical protocol, with some minor modifications, as outlined by the U.S. DOE for testing catalyst durability under membrane electrode assembly (MEA) conditions.<sup>75</sup> In particular, the potential is swept from 0.6 to 1.0 V for a total of 20 000 cycles, with the nanostructures supported

on a GCE immersed in 0.1 M HClO<sub>4</sub> so as to bracket the relevant potentials for ORR in a working fuel cell. However, care must be taken when comparing these values to those obtained under MEA conditions, since half-cell conditions, although very similar, are not exactly identical to MEA conditions. On the basis of this protocol, the ESA and activity of our nanostructures could be independently monitored by obtaining CVs and polarization curves after 5 000 cycles of operation. We have previously discussed the stability of ultrathin 2 nm Pt–Pd NW/C composites in detail.<sup>19</sup> In this section, results are shown for the submicrometer (Figure 8A) and the nanosized (Figure 8B) Pt–Pd NW samples, respectively, as a function of the percentage of ESA and specific activity over the course of these 20 000 cycles of operation.

As expected, the durability testing results show a decline in both the surface area and activity of the nanostructures over the course of the simulated lifetime. In the case of the surface area, the submicrometer and nanosized Pt–Pd NWs retained 60.2% and 89.7% of their ESA, respectively, after 20 000 cycles. The observed trends in ESA decline can be attributed to a restructuring of the catalysts during the durability test. Based upon representative TEM images of the structures collected after 20 000 cycles, the submicrometer and nanosized structures largely maintain their 1D morphology. However, it is apparent that the nanosized wires evolve a textured and roughened high surface area porous structure, wherein the overall wire is composed of interconnected crystallites with nanoporous voids. The evolution of porosity in the submicrometer nanostructures is also apparent. However, analysis of many examples of these wires reveals that the effect is less substantial. Presumably, the formation of porous structures results from the preferential dissolution of the less noble Pd from the core of the nanostructures, which has been demonstrated to be the primary mechanism for ESA loss in analogous Pt–Pd NPs.<sup>76</sup> Notwithstanding, the evolution of a highly porous structure in combination with significant nanoparticle formation in the case of the nanosized wires results in a higher proportional ESA after cycling, as compared with the submicrometer structures. In the case of the specific activity, the submicrometer and nanosized Pt–Pd NWs retained ~80.5% and 60.3% of their specific activity, respectively, after 20 000 cycles. The proportionally higher loss of specific activity associated with nanosized wires is not surprising given the significant morphological restructuring of the catalyst,

during the cycling process. Specifically, the evolution of a porous particulate structure in combination with the formation of NPs is expected to increase the number of defect sites significantly, thereby decreasing the catalyst's activity toward the ORR process.

## CONCLUSIONS

In this report, we have prepared submicrometer (270 nm) and nanosized (45 nm) Pd NWs utilizing a template-based approach that is not only sustainable but also allows for the preparation of high-quality nanostructures with predictable dimensions. The NWs in this case are largely single-crystalline and have been found to grow uniformly along the [110] crystallographic direction. We observe that the growth of the NWs proceeds by two steps, wherein initially a polycrystalline segment is formed by rapid reduction and nucleation. Subsequently, we believe that the NW growth continues through an electrodeposition process in a second step, resulting in the formation of a single-crystalline segment.

The ORR activity of optimized submicrometer and nanosized Pd NWs was determined electrochemically and compared with the activity of ultrathin 2 nm Pd NW/C samples, which revealed a distinctive size-dependent electrocatalytic enhancement of nearly 2-fold as the wire diameter was decreased. After the deposition of a Pt monolayer onto the Pd NW substrates, the core–shell Pt–Pd NWs displayed a similar size-dependent enhancement of nearly 2-fold in both specific activity and platinum mass activity. Thus, this current report demonstrates that the diameter-dependent enhancement in ORR activity can be generalized from not only Pt but also, for the first time, to Pd and Pt–Pd core–shell structures. We believe that the observed size-dependent trend results from a diameter-dependent contraction of the Pd NW surface as the diameter is decreased, an observation which is expected to increase the inherent ORR activity.

Hence, the observed size-dependent trend reported herein is of great interest, since it starkly contrasts with the trend observed in analogous 0D NP catalysts. Hence, the activity in 1D structures can be optimized by decreasing the diameter, which has the added benefit of maximizing the precious metal loading of these catalysts. More importantly, we expect that this size-dependent property can be further generalized to include alloyed, segmented, and hierarchical metallic NWs, which will allow for further optimization of activity.

## MATERIALS AND METHODS

**Synthesis of Palladium Nanowires.** The synthesis of submicrometer (270 nm) and nanosized (45 nm) palladium nanowires (Pd NWs) was accomplished by utilizing a U-tube double diffusion device. Specifically, sodium hexachloropalladate hydrate

(87.5 mg Na<sub>2</sub>PdCl<sub>6</sub>·xH<sub>2</sub>O, Alfa Aesar 99.9%) was dissolved in 5 mL of absolute ethanol in order to create a saturated precursor solution. Separately, a 5 mM sodium borohydride (NaBH<sub>4</sub>, Alfa Aesar 98%) solution was prepared by dissolving the solid powder into 5 mL of ethanol with a brief period of sonication

in order to create a reducing agent solution. Immediately prior to performing the reaction, commercially available polycarbonate membranes (Whatman, Nucleopore track etched) with pore sizes of either 200 or 15 nm were sonicated in ethanol to presaturate the pores with solvent.

The ethanol saturated membranous template was clamped between the two half-cells of the U-tube device and the half-cells were separately filled with precursor and reducing agent solutions, respectively, as shown in Supporting Information, Figure S2. After 16 min of reaction time, the reaction completion was signaled by the visible formation of metallic material on the exterior surfaces of the template; the filled template membrane was then removed from the U-tube and gently rinsed with ethanol. Residual metal present on the external surfaces of the template was physically removed by polishing the template on a commercially available, soft Arkansas Wet-Stone (Tools for Working Wood Company, Brooklyn, NY) with mineral oil serving as a lubricant. The PC template itself was dissolved away by immersing the membrane in methylene chloride for a minimum of 15 min and isolated by centrifugation. These washing and isolating steps were repeated several times to ensure complete removal of residual PC. Subsequently, purified isolated NWs could be obtained by washing the gray-black powder in ethanol. A final catalyst ink was prepared by dispersing the powder into 25% isopropyl alcohol (IPA) in water. Free standing arrays of the NWs could be obtained by affixing the template onto a Si wafer with double-sided Cu tape and exposing the wafer to an oxygen plasma for a total of 20 min in a reactive ion etcher (March Plasma).

The synthesis of carbon-supported ultrathin (2 nm) palladium nanowires (Pd NW/C) has been described in detail in a previous report.<sup>19</sup> To summarize, a mixture of palladium nitrate (Alfa Aesar, 99.9%), octadecylamine (Acros Organics, 90%), and dodecyltrimethylammonium bromide (TCI, >99%) in toluene was reduced by a solution of NaBH<sub>4</sub> under an inert atmosphere. The resulting NWs were subsequently isolated and supported onto conductive carbon (Vulcan XC-72, Cabot) by sonicating the mixture of NWs and carbon mutually dispersed into chloroform. The composites were subsequently removed from the chloroform, washed with hexanes, and finally transferred onto ultraclean silicon wafers for a gas-phase UV-generated ozone treatment. As-treated NWs were removed from the wafers by sonication in a 25% IPA solution in order to create the corresponding catalyst ink.

**Characterization.** The morphology and structural quality of as-prepared Pd NWs were initially characterized by scanning electron microscopy (SEM). SEM samples were prepared by dispersing the relevant Pd NW powder into ethanol by a brief period of sonication and drop-casting the resulting dispersion onto cleaned Si wafers. Images were obtained by utilizing field emission electron microscopes (Leo 1550 and Hitachi S4800) at an operating voltage of 15 and 5 kV, respectively. Subsequently, low-magnification transmission electron microscopy (TEM) images were obtained at 80 kV on a Technai12 BioTwinG<sup>2</sup> instrument (FEI), equipped with an AMT XR-60 CCD camera system. Cross sections of the template were prepared by embedding the as-prepared membranes in either Spurr or Epon resin, and ultrathin sections of 80 nm in thickness were cut with a Reichert-Jung UltracutE ultramicrotome and placed onto Formvar coated slot copper grids. High-resolution TEM (HRTEM) images, selected area electron diffraction (SAED) patterns, and energy dispersive analysis (EDAX) spectra were acquired using a FEI Titan 80-300 TEM equipped with a Cs-corrector, operated at 300 kV. TEM samples of individual NWs were prepared by dispersing the Pd NWs in ethanol and evaporating a single drop onto a 300 mesh Cu grid, coated with a lacey carbon film.

Powder X-ray diffraction (XRD) patterns were obtained using Cu K $\alpha$  radiation ( $\lambda = 1.5 \text{ \AA}$ ) at a scan rate of  $0.4^\circ$  in  $2\theta$  per minute intervals, utilizing a Scintag diffractometer operating in the Bragg–Brentano configuration. XRD samples were prepared by rendering the Pd NWs into a slurry with a minimal amount of ethanol and allowing to air-dry.

**Electrochemistry and Platinum Monolayer Deposition.** Electrochemical measurements and Pt monolayer deposition were

performed with the submicrometer-sized and nanometer-sized Pd NW samples supported onto a thin layer of conductive carbon in order to maximize the distribution of the catalyst on the electrode surface. Specifically, a  $5 \mu\text{L}$  aliquot of a 1 mg/mL solution of Vulcan XC-72 dispersed in 25% IPA solution was placed onto a polished glassy carbon electrode (GCE) (RDE, Pine Instruments, 5 mm active area) and dried under vacuum in order to create a uniform layer of carbon. Later, a  $5 \mu\text{L}$  drop of the appropriate catalyst ink was subsequently placed onto the carbon-modified electrode and allowed to dry under vacuum. Electrochemical measurements were obtained in a 0.1 M perchloric acid solution (HClO<sub>4</sub>, Fisher Scientific, Optima grade), prepared with ultrapure water. Unless otherwise mentioned, an Ag/AgCl electrode (3 M Cl<sup>-</sup>) isolated in a double junction chamber (Cypress) and a platinum foil served as the reference electrode and counter-electrode, respectively. All potentials recorded in this paper have been measured with respect to the reversible hydrogen electrode (RHE), unless otherwise noted.

The deposition of a Pt monolayer onto the Pd NW surface was accomplished by initially electrodepositing a monolayer of Cu through Cu underpotential deposition (UPD) followed by galvanic displacement of the Cu adatoms by Pt.<sup>69,77</sup> The deposition of a Cu monolayer (Cu UPD) was achieved in a solution of 50 mM CuSO<sub>4</sub> in a 0.10 M H<sub>2</sub>SO<sub>4</sub> electrolyte.<sup>66</sup> The Cu modified electrode was then transferred to a solution of 1.0 mM K<sub>2</sub>PtCl<sub>6</sub> dissolved in 50 mM H<sub>2</sub>SO<sub>4</sub> and immersed for a minimum of 5 min. All of these steps were performed in a custom-made two-chamber glass housing, allowing for the transfer of the Cu modified electrode under an inert N<sub>2</sub> atmosphere so as to prevent the oxidation of the Cu adatoms. After deposition of the Pt monolayer, the electrode is removed from the glass housing, washed thoroughly with ultrapure water to remove sulfate impurities, and covered with a  $5 \mu\text{L}$  drop of Nafion solution (0.025% in ethanol), prepared from a commercially available stock solution (5%, Aldrich).

A similar procedure has been utilized for the preparation of ultrathin Pd NW/C and commercial catalysts with only minor modifications. For example, in the case of the ultrathin Pd NW/C catalyst, a  $5 \mu\text{L}$  drop of the catalyst ink was placed directly onto a polished GCE without prior addition of a carbon layer. The residual surfactant present in this case could be readily removed by utilizing a selective CO adsorption process, that has been described in detail elsewhere.<sup>19</sup> After cleaning, a Pt monolayer was deposited utilizing the aforementioned procedure for the Pd NW samples. The commercial carbon-supported Pt and Pd catalysts (20% loading, Etek) were rendered into 2 mg/mL catalyst inks in 25% IPA, and subsequently a  $5 \mu\text{L}$  drop of the catalyst ink was placed directly onto a polished GCE.

**Measurement of ORR Activity and Catalyst Durability.** Studies of the submicrometer and nanosized Pd NW samples and ultrathin Pd NW/C composites were performed utilizing the thin-layer rotating disk electrode (RDE) method.<sup>78</sup> Initially, cyclic voltammetry (CV) was performed in a deoxygenated 0.1 M HClO<sub>4</sub> solution with a scan rate of 20 mV/s so as to determine the electrochemically addressable surface area (ESA). Polarization curves were then obtained in an oxygen-saturated 0.1 M HClO<sub>4</sub> solution, maintained at 20 °C with a scan rate of 10 mV/s and a rotation speed of 1600 rpm. The measured ORR activity of the various Pd NW and Pt–Pd NW samples was compared with that of commercial Pd/C and Pt/C, respectively. The longevity of the various catalysts was studied under half-cell conditions in perchloric acid by utilizing a durability test described by the U.S. DOE for simulating a catalyst lifetime under MEA conditions.<sup>75</sup> Specifically, the electrode was cycled from 0.6 to 1.0 V at 50 mV/s in a 0.1 M HClO<sub>4</sub> solution. During the course of the durability test, the cell was left open to the atmosphere in order to allow for replenishment of the dissolved oxygen in the electrolyte. The ESA and specific activity (electrochemical surface area activity, ECSA) were obtained after every 5 000 cycles for a total of 20 000 cycles. By means of comparison, identical durability measurements were obtained on commercial high performance Pt NP/C (20%, Etek).

**Acknowledgment.** Research (including support for S.S.W. and electrochemical experiments) was supported by the U.S. Department of Energy, Basic Energy Sciences, Materials Sciences and Engineering Division. We especially acknowledge Dr. R. Adzic and his group's assistance and guidance with all of the electrochemical and electrocatalytic experiments reported herein. We also thank J. Patete for relevant discussions and assistance with the preparation of the manuscript. In addition, we thank Dr. J. Quinn for his assistance with obtaining FE-SEM images. We also acknowledge S. Van Horn at the Central Microscopy Imaging Center at Stony Brook for her assistance with preparing the microtome cross sections. We performed experiments at the Center for Functional Nanomaterials located at Brookhaven National Laboratory, which is supported by the U.S. Department of Energy under Contract No. DE-AC02-98CH10886.

**Supporting Information Available:** Supporting figures along with additional characterization (e.g., microscopy and diffraction images as well as electrochemical data) of our Pd NWs, schematics of the U-tube synthesis protocol, an explanation of electrochemical methods, and further insights into the growth mechanism of the Pd NWs. This material is available free of charge via the Internet at <http://pubs.acs.org>.

## REFERENCES AND NOTES

- Tiano, A. L.; Koenigsmann, C.; Santulli, A. C.; Wong, S. S. Solution-Based Synthetic Strategies for One-Dimensional Metal-Containing Nanostructures. *Chem. Commun.* **2010**, *46*, 8093–8130.
- Koenigsmann, C.; Wong, S. S. One-Dimensional Noble Metal Electrocatalysts: A Promising Structural Paradigm for Direct Methanol Fuel Cells. *Energy Environ. Sci.* **2011**, *4*, 1161–1176.
- Antolini, E.; Perez, J. The Renaissance of Unsupported Nanostructured Catalysts for Low-Temperature Fuel Cells: From the Size to the Shape of Metal Nanostructures. *J. Mater. Sci.* **2011**, *1*–23.
- Morozan, A.; Jousseline, B.; Palacin, S. Low-Platinum and Platinum-Free Catalysts for the Oxygen Reduction Reaction at Fuel Cell Cathodes. *Energy Environ. Sci.* **2011**, *4*, 1238–1254.
- Nørskov, J. K.; Rossmeisl, J.; Logadottir, A.; Lindqvist, L.; Kitchin, J. R.; Bligaard, T.; Jonsson, H. Origin of the Overpotential for Oxygen Reduction at a Fuel-Cell Cathode. *J. Phys. Chem. B* **2004**, *108*, 17886–17892.
- Wang, J. X.; Zhang, J.; Adzic, R. R. Double-Trap Kinetic Equation for the Oxygen Reduction Reaction on Pt(111) in Acidic Media. *J. Phys. Chem. A* **2007**, *111*, 12702–12710.
- He, C.; Desai, S.; Brown, G.; Bollepalli, S. PEM Fuel Cell Catalysts: Cost, Performance, and Durability. *Electrochem. Soc. Interface* **2005**, *14*, 41–44.
- Gewirth, A. A.; Thorum, M. S. Electrocatalysis of Dioxygen for Fuel-Cell Applications: Materials and Challenges. *Inorg. Chem.* **2010**, *49*, 3557–3566.
- Markovic, N. M.; Ross, P. N. Electrocatalysts at Well Defined Surfaces: Kinetics of Oxygen Reduction and Hydrogen Oxidation/Evolution on Pt (*hkl*) Electrodes. In *Interfacial Electrochemistry: Theory, Experiment and Applications*; Wieckowski, A., Ed.; Marcel Dekker, Inc: New York, 1999; Vol. 1, pp 821–841.
- Williams, M. C. Status and Promise of Fuel Cell Technology. *Fuel Cells* **2001**, *1*, 87–91.
- Markovic, N. M.; Schmidt, T. J.; Stamenković, V.; Ross, P. N. Oxygen Reduction Reaction on Pt and Pt Bimetallic Surfaces: A Selective Review. *Fuel Cells* **2001**, *1*, 105–116.
- Sinha, J.; Marcinkoski, J.; Randolph, K.; Benjamin, T. G. Cost Analysis of Fuel Cell Stacks/Systems; DOE Hydrogen Program Review: Arlington, VA, 2009.
- Xia, Y.; Yang, P.; Sun, Y.; Wu, Y.; Mayers, B.; Gates, G.; Yin, Y.; Kim, F.; Yan, H. One-Dimensional Nanostructures: Synthesis, Characterization, and Applications. *Adv. Mater.* **2003**, *15*, 353–389.
- Cademartiri, L.; Ozin, G. A. Ultrathin Nanowires—A Materials Chemistry Perspective. *Adv. Mater.* **2009**, *21*, 1013–1020.
- Sun, S.; Jaouen, F.; Dodelet, J.-P. Controlled Growth of Pt Nanowires on Carbon Nanospheres and Their Enhanced Performance as Electrocatalysts in PEM Fuel Cells. *Adv. Mater.* **2008**, *20*, 3900–3904.
- Górny, M. Ł.; Walton, A. S.; Evans, S. D. Synthesis of High-Surface-Area Platinum Nanotubes Using a Viral Template. *Adv. Funct. Mater.* **2010**, *20*, 1295–1300.
- Liang, H.-W.; Cao, X.; Zhou, F.; Cui, C.-H.; Zhang, W.-J.; Yu, S.-H. Free-Standing Pt-Nanowire: A Membrane as a Highly Stable Electrocatalyst for the Oxygen Reduction Reaction. *Adv. Mater.* **2011**, *23*, 1467–1471.
- Xiao, L.; Zhuang, L.; Liu, Y.; Lu, J.; Abruna, H. D. Activating Pd by Morphology Tailoring for Oxygen Reduction. *J. Am. Chem. Soc.* **2008**, *131*, 602–608.
- Koenigsmann, C.; Santulli, A. C.; Gong, K.; Vukmirovic, M. B.; Zhou, W.-p.; Sutter, E.; Wong, S. S.; Adzic, R. R. Enhanced Electrocatalytic Performance of Processed, Ultrathin, Supported Pd–Pt Core–Shell Nanowire Catalysts for the Oxygen Reduction Reaction. *J. Am. Chem. Soc.* **2011**, *133*, 9783–9795.
- Chen, Z.; Waje, M.; Li, W.; Yan, Y. Supportless Pt and PtPd Nanotubes as Electrocatalysts for Oxygen-Reduction Reactions. *Angew. Chem., Int. Ed.* **2007**, *46*, 4060–4063.
- Zhiyong, Z.; Li, M.; Wu, Z.; Li, W. Ultra-Thin PtFe-Nanowires as Durable Electrocatalysts for Fuel Cells. *Nanotechnology* **2011**, *22*, 015602/1–5.
- Zhou, H.; Zhou, W.-p.; Adzic, R. R.; Wong, S. S. Enhanced Electrocatalytic Performance of One-Dimensional Metal Nanowires and Arrays Generated via an Ambient, Surfactantless Synthesis. *J. Phys. Chem. C* **2009**, *113*, 5460–5466.
- Koenigsmann, C.; Zhou, W.-p.; Adzic, R. R.; Sutter, E.; Wong, S. S. Size-Dependent Enhancement of Electrocatalytic Performance in Relatively Defect-Free, Processed Ultrathin Platinum Nanowires. *Nano Lett.* **2010**, *10*, 2806–2811.
- Diao, J.; Gall, K.; Dunn, M. L. Surface-Stress-Induced Phase Transformation in Metal Nanowires. *Nat. Mater.* **2003**, *2*, 656–660.
- Haftel, M. I.; Gall, K. Density Functional Theory Investigation of Surface-Stress-Induced Phase Transformations in fcc Metal Nanowires. *Phys. Rev. B: Condens. Matter* **2006**, *74*, 035420–035412.
- Kondo, Y.; Takayanagi, K. Synthesis and Characterization of Helical Multishell Gold Nanowires. *Science* **2000**, *289*, 606–608.
- Xiong, Y.; Xia, Y. Shape-Controlled Synthesis of Metal Nanostructures: The Case of Palladium. *Adv. Mater.* **2007**, *19*, 3385–3391.
- Huang, X.; Zheng, N. One-Pot, High-Yield Synthesis of 5-Fold Twinned Pd Nanowires and Nanorods. *J. Am. Chem. Soc.* **2009**, *131*, 4602–4603.
- Teng, X.; Han, W.; Ku, W.; Hucker, M. Synthesis of Ultrathin Palladium and Platinum Nanowires and a Study of their Magnetic Properties. *Angew. Chem., Int. Ed.* **2008**, *47*, 2055–2058.
- Song, Y.; Garcia, R. M.; Dorin, R. M.; Wang, H.; Qiu, Y.; Coker, E. N.; Steen, W. A.; Miller, J. E.; Shelnutt, J. A. Synthesis of Platinum Nanowire Networks Using a Soft Template. *Nano Lett.* **2007**, *7*, 3650–3655.
- Ksar, F. a.; Surendran, G.; Ramos, L.; Keita, B.; Nadjo, L.; Prouzet, E.; Beaunier, P.; Hagège, A. s.; Audonnet, F.; Remita, H. Palladium Nanowires Synthesized in Hexagonal Mesophases: Application in Ethanol Electrooxidation. *Chem. Mater.* **2009**, *21*, 1612–1617.
- Caihong, F.; Zhang, R.; Yin, P.; Li, L.; Guo, L.; Shen, Z. Direct Solution Synthesis of Pd Nanowire Networks and Their Application in Surface-Enhanced Raman Scattering. *Nanotechnology* **2008**, *19*, 305601/1–8.
- Liang, H.-W.; Liu, S.; Gong, J.-Y.; Wang, S.-B.; Wang, L.; Yu, S.-H. Ultrathin Te Nanowires: An Excellent Platform for Controlled Synthesis of Ultrathin Platinum and Palladium Nanowires/Nanotubes with Very High Aspect Ratio. *Adv. Mater.* **2009**, *21*, 1850–1854.

34. Yuan, Q.; Zhou, Z.; Zhuang, J.; Wang, X. Seed Displacement, Epitaxial Synthesis of Rh/Pt Bimetallic Ultrathin Nanowires for Highly Selective Oxidizing Ethanol to CO<sub>2</sub>. *Chem. Mater.* **2010**, *22*, 2395–2402.
35. Yuan, Q.; Zhuang, J.; Wang, X. Single-Phase Aqueous Approach Toward Pd Sub-10 nm Nanocubes and Pd–Pt Heterostructured Ultrathin Nanowires. *Chem. Commun.* **2009**, *6613*–6615.
36. Lu, Y.; Wang, Y.; Chen, W. Silver Nanorods for Oxygen Reduction: Strong Effects of Protecting Ligand on the Electrocatalytic Activity. *J. Power Sources* **2011**, *196*, 3033–3038.
37. Hurst, S. J.; Payne, E. K.; Qin, L.; Mirkin, C. A. Multisegmented One-Dimensional Nanorods Prepared by Hard-Template Synthetic Methods. *Angew. Chem., Int. Ed.* **2006**, *45*, 2672–2692.
38. Kline, T. R.; Tian, M.; Wang, J.; Sen, A.; Chan, M. W. H.; Mallouk, T. E. Template-Grown Metal Nanowires. *Inorg. Chem.* **2006**, *45*, 7555–7565.
39. Liang, H.-W.; Liu, S.; Yu, S.-H. Controlled Synthesis of One-Dimensional Inorganic Nanostructures Using Pre-existing One-Dimensional Nanostructures as Templates. *Adv. Mater.* **2010**, *22*, 3925–3937.
40. Perry, J. L.; Martin, C. R.; Stewart, J. D. Drug-Delivery Strategies by Using Template-Synthesized Nanotubes. *Chem.—Eur. J.* **2011**, *17*, 6296–6302.
41. Chen, A.; Holt-Hindle, P. Platinum-Based Nanostructured Materials: Synthesis, Properties, and Applications. *Chem. Rev.* **2010**, *110*, 3767–3804.
42. Wang, H.; Xu, C.; Cheng, F.; Jiang, S. Pd Nanowire Arrays as Electrocatalysts for Ethanol Electrooxidation. *Electrochem. Commun.* **2007**, *9*, 1212–1216.
43. Zhang, F.; Yiu, Y.; Aronson, M. C.; Wong, S. S. Exploring the Room-Temperature Synthesis and Properties of Multifunctional Doped Tungstate Nanorods. *J. Phys. Chem. C* **2008**, *112*, 14816–14824.
44. Zhang, F.; Wong, S. S. Ambient Large-Scale Template-Mediated Synthesis of High-Aspect Ratio Single-Crystalline, Chemically Doped Rare-Earth Phosphate Nanowires for Bioimaging. *ACS Nano* **2009**, *4*, 99–112.
45. Zhang, F.; Wong, S. S. Controlled Synthesis of Semiconducting Metal Sulfide Nanowires. *Chem. Mater.* **2009**, *21*, 4541–4554.
46. Zhang, F.; Sfeir, M. Y.; Misewich, J. A.; Wong, S. S. Room-Temperature Preparation, Characterization, and Photoluminescence Measurements of Solid Solutions of Various Compositionally-Defined Single-Crystalline Alkaline-Earth-Metal Tungstate Nanorods. *Chem. Mater.* **2008**, *20*, 5500–5512.
47. Zhang, F.; Mao, Y.; Park, T.-J.; Wong, S. S. Green Synthesis and Property Characterization of Single-Crystalline Perovskite Fluoride Nanorods. *Adv. Funct. Mater.* **2008**, *18*, 103–112.
48. Mao, Y.; Zhang, F.; Wong, S. Ambiant Template-Directed Synthesis of Single-Crystalline Alkaline-Earth Metal Fluoride Nanowires. *Adv. Mater.* **2006**, *18*, 1895–1899.
49. Mao, Y.; Wong, S. S. General, Room-Temperature Method for the Synthesis of Isolated as Well as Arrays of Single-Crystalline ABO<sub>4</sub>-Type Nanorods. *J. Am. Chem. Soc.* **2004**, *126*, 15245–15252.
50. Patete, J. M.; Peng, X.; Koenigsmann, C.; Xu, Y.; Karn, B.; Wong, S. S. Viable Methodologies for the Synthesis of High-Quality Nanostructures. *Green Chem.* **2011**, *13*, 482–519.
51. Schönenberger, C.; van der Zande, B. M. I.; Fokkink, L. G. J.; Henny, M.; Schmid, C.; Krüger, M.; Bachtold, A.; Huber, R.; Birk, H.; Staufer, U. Template Synthesis of Nanowires in Porous Polycarbonate Membranes: Electrochemistry and Morphology. *J. Phys. Chem. B* **1997**, *101*, 5497–5505.
52. Favier, F.; Walter, E. C.; Zach, M. P.; Benter, T.; Penner, R. M. Hydrogen Sensors and Switches from Electrodeposited Palladium Mesowire Arrays. *Science* **2001**, *293*, 2227–2231.
53. Yun, M.; Myung, N. V.; Vasquez, R. P.; Lee, C.; Menke, E.; Penner, R. M. Electrochemically Grown Wires for Individually Addressable Sensor Arrays. *Nano Lett.* **2004**, *4*, 419–422.
54. Cheng, F.; Wang, H.; Sun, Z.; Ning, M.; Cai, Z.; Zhang, M. Electrodeposited Fabrication of Highly Ordered Pd Nanowire Arrays for Alcohol Electrooxidation. *Electrochim. Commun.* **2008**, *10*, 798–801.
55. Kartopu, G.; Habouti, S.; Es-Souni, M. Synthesis of Palladium Nanowire Arrays with Controlled Diameter and Length. *Mater. Chem. Phys.* **2008**, *107*, 226–230.
56. Sharabani, R.; Reuveni, S.; Noy, G.; Shapira, E.; Sadeh, S.; Selzer, Y. Fabrication of Very High Aspect Ratio Metal Nanowires by a Self-Propulsion Mechanism. *Nano Lett.* **2008**, *8*, 1169–1173.
57. Cui, S. T. Molecular Self-Diffusion in Nanoscale Cylindrical Pores and Classical Fick's Law Predictions. *J. Chem. Phys.* **2005**, *123*, 054706–054704.
58. Crank, J. *The Mathematics of Diffusion*; Oxford University Press: Oxford, UK, 1975.
59. Kondo, S.; Nakamura, M.; Maki, N.; Hoshi, N. Active Sites for the Oxygen Reduction Reaction on the Low and High Index Planes of Palladium. *J. Phys. Chem. C* **2009**, *113*, 12625–12628.
60. Shao, M.; Yu, T.; Odell, J. H.; Jin, M.; Xia, Y. Structural Dependence of Oxygen Reduction Reaction on Palladium Nanocrystals. *Chem. Commun.* **2011**, *47*, 6566–6568.
61. Koper, M. T. M. *Fuel Cell Catalysts*; Wiley Interscience: Hoboken, NJ, 2009; p 712.
62. Fiorentini, V.; Methfessel, M.; Scheffler, M. Reconstruction Mechanism of fcc Transition Metal (001) Surfaces. *Phys. Rev. Lett.* **1993**, *71*, 1051–1054.
63. van Beurden, P.; Kramer, G. J. Atomistic Mechanisms for the (1 × 1) to Hex Surface Phase Transformations of Pt(100). *J. Chem. Phys.* **2004**, *121*, 2317–2325.
64. Kondo, Y.; Takayanagi, K. Gold Nanobridge Stabilized by Surface Structure. *Phys. Rev. Lett.* **1997**, *79*, 3455–3458.
65. Adzic, R.; Zhang, J.; Sasaki, K.; Vukmirovic, M.; Shao, M.; Wang, J.; Nilekar, A.; Mavrikakis, M.; Valerio, J.; Uribe, F. Platinum Monolayer Fuel Cell Electrocatalysts. *Top. Catal.* **2007**, *46*, 249–262.
66. Wang, J. X.; Inada, H.; Wu, L.; Zhu, Y.; Choi, Y.; Liu, P.; Zhou, W.-P.; Adzic, R. R. Oxygen Reduction on Well-Defined Core–Shell Nanocatalysts: Particle Size, Facet, and Pt Shell Thickness Effects. *J. Am. Chem. Soc.* **2009**, *131*, 17298–17302.
67. Rossmeisl, J.; Nørskov, J. K. Electrochemistry on the Computer: Understanding How to Tailor the Metal Overlays for the Oxygen Reduction Reaction. *Surf. Sci.* **2008**, *602*, 2337–2338.
68. Zhang, J.; Lima, F. H. B.; Shao, M. H.; Sasaki, K.; Wang, J. X.; Hanson, J.; Adzic, R. R. Platinum Monolayer on Non-noble Metal-Noble Metal Core–Shell Nanoparticle Electrocatalysts for O<sub>2</sub> Reduction. *J. Phys. Chem. B* **2005**, *109*, 22701–22704.
69. Zhang, J.; Mo, Y.; Vukmirovic, M. B.; Klie, R.; Sasaki, K.; Adzic, R. R. Platinum Monolayer Electrocatalysts for O<sub>2</sub> Reduction: Pt Monolayer on Pd(111) and on Carbon-Supported Pd Nanoparticles. *J. Phys. Chem. B* **2004**, *108*, 10955–10964.
70. Wang, S.; Jiang, S. P.; Wang, X.; Guo, J. Enhanced Electrochemical Activity of Pt Nanowire Network Electrocatalysts for Methanol Oxidation Reaction of Fuel Cells. *Electrochim. Acta* **2011**, *56*, 1563–1569.
71. Maillard, F.; Savinova, E. R.; Stimming, U. CO Monolayer Oxidation on Pt Nanoparticles: Further Insights into the Particle Size Effects. *J. Electroanal. Chem.* **2007**, *599*, 221–232.
72. Maillard, F.; Eikerling, M.; Cherstiouk, O. V.; Schreier, S.; Savinova, E.; Stimming, U. Size Effects on Reactivity of Pt Nanoparticles in CO Monolayer Oxidation: The Role of Surface Mobility. *Faraday Discuss.* **2004**, *125*, 357–377.
73. Greeley, J.; Nørskov, J. K. Combinatorial Density Functional Theory-Based Screening of Surface Alloys for the Oxygen Reduction Reaction. *J. Phys. Chem. C* **2009**, *113*, 4932–4939.
74. Zhang, J.; Vukmirovic, M. B.; Xu, Y.; Mavrikakis, M.; Adzic, R. R. Controlling the Catalytic Activity of Platinum-Monolayer Electrocatalysts for Oxygen Reduction with Different Substrates. *Angew. Chem., Int. Ed.* **2005**, *44*, 2132–2135.

75. Multi-Year Research, Development and Demonstration Plan: Planned Program Activities for 2005–2015; Department of Energy: Washington, DC, **2009**.
76. Sasaki, K.; Naohara, H.; Cai, Y.; Choi, Y. M.; Liu, P.; Vukmirovic, M. B.; Wang, J. X.; Adzic, R. R. Core-Protected Platinum Monolayer Shell High-Stability Electrocatalysts for Fuel-Cell Cathodes. *Angew. Chem., Int. Ed.* **2010**, *49*, 8602–8607.
77. Brankovic, S. R.; Wang, J. X.; Adzic, R. R. Metal Monolayer Deposition by Replacement of Metal Adlayers on Electrode Surfaces. *Surf. Sci.* **2001**, *474*, L173–L179.
78. Garsany, Y.; Baturina, O. A.; Swider-Lyons, K. E.; Kocha, S. S. Experimental Methods for Quantifying the Activity of Platinum Electrocatalysts for the Oxygen Reduction Reaction. *Anal. Chem.* **2010**, *82*, 6321–6328.